Plasma Sources Science and Technology

Check for updates

PAPER

OPEN ACCESS

RECEIVED
13 April 2026

REVISED
12 June 2026

ACCEPTED FOR PUBLICATION
15 July 2026

PUBLISHED
24 August 2026

Original content from this work may be used under the terms of the Creative Commons Attribution 4.0 licence.

Any further distribution of this work must maintain attribution to the author(s) and the title of the work, journal citation and DOI.

Effects of nitrogen addition to argon gas on the excited level kinetics and the optical emission from a capacitively coupled plasma

Zoltán Donkó[1,2,*], **Simon Chouteau**[2,5], **Tsanko V Tsankov**[3], **Fatima Jenina Arellano**[4], **Satoshi Hamaguchi**[2] **and Peter Hartmann**[1]

[1] Institute for Solid State Physics and Optics, HUN-REN Wigner Research Centre for Physics, 1121 Budapest, Konkoly Thege Miklós str. 29-33, Hungary
[2] R^3 Institute of Newly-Emerging Science Design (INSD), The University of Osaka, Osaka 565-0871, Japan
[3] Laboratoire de Physique des Plasmas (LPP), École Polytechnique, CNRS, Sorbonne Universite, Institut Polytechnique de Paris, Palaiseau 91128, France
[4] Graduate School of Engineering, The University of Osaka, Osaka 565-0871, Japan
[5] JSPS International Research Fellow P24751.
[*] Author to whom any correspondence should be addressed.

E-mail: donko.zoltan@wigner.hun-ren.hu

Keywords: capacitively coupled plasma, gas mixtures, excited level kinetics, optical spectroscopy

Abstract

The effect of a nitrogen admixture to argon gas, on the densities of the Ar $1s_5$ and $1s_3$ metastable atoms and the intensities of Ar $2p\rightarrow 1s$ spectral lines (in Paschen notation) radiated by a capacitively coupled plasma is investigated experimentally and by a computational model comprising particle simulation of the discharge and a fluid (diffusion-reaction-radiation) description for the excited Ar atoms. The nitrogen admixture has a twofold effect on the plasma and its radiation processes: N_2 molecules (i) efficiently quench excited Ar atoms thereby influencing their densities and thus also the ionization and excitation balance, and (ii) due to the lower threshold energy for inelastic excitation channels, the high-energy part of the electron energy probability function is strongly depleted. Both of these effects result in significant changes of the Ar-I emission spectrum due to the roles of the excited (Ar 1s) atoms in the stepwise excitation, and of the high-energy electrons in the direct excitation of Ar 2p levels from which the investigated transitions originate. The simulations make it possible to separate these two contributions and to reveal the excitation and depopulation pathways of the excited Ar-I levels. Experimentally, the densities of the Ar $1s_5$ and $1s_3$ metastable atoms are measured with tunable diode laser absorption spectroscopy while the Ar $2p\rightarrow 1s$ spectral line intensities are acquired with conventional optical emission spectroscopy (with relative calibration). The computational results are found to be in fair agreement with these measured quantities over the whole range of parameters considered ($p = 2.5$–40 Pa, $[N_2] = 0\%$–5%) thus confirming the conclusions from the simulations.

1. Introduction

Ar/N_2 discharges created in various plasma sources, under a wide variety of conditions have been the subject of numerous investigations in the past. In [1], the radial density profile of Ar $1s_5$ metastable atoms in the positive column of a DC glow discharge was studied. A significant decrease of the Ar metastable atom population due to nitrogen addition was found to be the consequence of two effects: (i) the efficient quenching collisions between Ar 1s level atoms and N_2 molecules (that lead to the formation of $N_2(B^3\Pi_g$ and $N_2(C^3\Pi_u)$ excited molecules, see, e.g. [2]) and (ii) the change of the shape of the electron energy probability function (EEPF) due to the lower-threshold-energy excitation channels of N_2, which efficiently depletes the tail of the EEPF resulting thereby in a lower population of the Ar excited levels. These effects act, in general, similarly in other plasma sources, as well. For example, [3]. reported

© 2026 The Author(s). Published by IOP Publishing Ltd

(line-integrated) densities of Ar atoms in all the four 1s excited levels in an inductively coupled plasma operated at pressures between 4 and 50 mTorr. A 50% nitrogen content in the gas resulted in a surprisingly low, factor of only about two decrease of the $1s_5$ density and about an order of magnitude density decrease of the $1s_4$ population. In [4], the reduction of Ar $1s_5$ metastable density as a consequence of the presence of N_2 was studied in an electron beam generated plasma using laser-induced fluorescence. In the absence of N_2, peak Ar metastable atom densities on the order of 10^{10} cm^{-3} were found, and a threefold decrease at a nitrogen concentration of ≈15% was measured at 60 mTorr operating pressure. A depletion of the $1s_5$ metastable atom density due to mixing N_2 to Ar was also observed recently in microwave discharges [5].

The optical emission from Ar and Ar+N_2 plasmas and the possibilities of determining plasma properties (electron density and electron temperature) have also been a subject of studies, see, e.g. [6–8] and references therein. Via the analysis of the multiple excitation and de-excitation pathways in such plasmas, the utilization of the line intensity ratio method, which can provide a non-intrusive way to determine plasma characteristics, has been analyzed in a number of works, e.g. [9–12] for argon and in [13–16] for nitrogen. Modifications to the kinetics of charged and excited species in a surface wave discharge, were revealed via changes of the optical emission spectrum in [17]. In [18], the dependence of the Ar-I 2p→ 1s spectral line intensities on the nitrogen content of the Ar/N_2 working gas of an electron beam sustained plasma was studied, up to 20% N_2 contents. The most significant line intensity reduction was found for the 811.5 nm and 763.5 nm transitions, which are known to be preferentially excited by stepwise electron-impact excitation from Ar 1s levels. The 750.4 nm line, known to be preferentially excited by electron-impact excitation of ground state Ar atoms, showed less reduction in intensity with increasing N_2 concentration.

Detailed insight into the kinetics of excited levels can be achieved by collisional radiative models (CRMs), which are based on balance equations for each of the excited levels considered, including both electron-collision-driven and radiative populating and depopulating mechanisms [19–26]. CRMs can be used primarily for diagnostic purposes by relating the experimental spectra to the plasma parameters such as the electron density and temperature [27].

In addition to the analysis of the light emission of argon lines, the emission of N_2 molecular bands can provide information about the plasma characteristics (like the rotational temperature of N_2 molecules, which is often considered to be a good approximation of the gas temperature, see. e.g. [28]). Ar 1s atom densities in Ar/N_2 discharges were derived based both on measurements of the second positive system of N_2 and intensities of the Ar 2p→ 1s spectral lines, in [29].

Other works have focused on the emission properties of a helical plasma source at moderate pressures (200–400 Pa) operating in Ar/N_2 mixtures [30], as well as the dissociation of N_2 molecules in inductively coupled Ar/N_2 plasmas [31]. A number of investigations have also been motivated by the important applications of Ar/N_2 plasmas, like thin film deposition [32, 33], e.g. by DC magnetron sputtering [34], the nitridation of metals and alloys in high-current hollow cathode discharges [35], as well as hazardous waste destruction in atmospheric-pressure arc discharges [36]. Medical and biological applications of plasma jets [37, 38] are based on the generation of radical species in plasmas of mixtures of noble gases and molecular gases, including Ar/N_2. Another important type of discharges where Ar–N_2 mixtures are present are the ones used for analytical glow discharge optical emission spectroscopy (OES) that allows analyzing the composition of samples (with depth profiling), via cathode sputtering and the measurement of the emitted radiation [39–41].

Regarding capacitively coupled plasmas (CCPs), in [42] a self-consistent fluid model was presented for Ar/N_2 discharges. Measurements of ion density were performed with a floating double probe and spectral line intensities from Ar 2p levels were measured. Good consistency was found between the numerical and experimental results. Atmospheric-pressure operation of Ar/N_2 CCPs was investigated in [43] by measuring the electrical characteristics, N atom formation and the generation of molecular excited levels as a function of N_2 concentration. Low-pressure Ar/N_2 CCPs under dual-frequency (8 MHz / 100 MHz) excitation were studied in [44] by particle-in-cell (PIC)/Monte Carlo collisions (PIC/MCCs) simulations and optical spectroscopy measurements.

In our previous studies, we have used a CRM to predict line intensities in an Ar CCP based on the computation of the electron density and the EEPF using PIC/MCCs simulation [45]. Subsequently, we have realized an iterative solution of (i) a PIC/MCC simulation extended by electron-impact processes between 30 excited Ar levels [46] to compute all electron-impact reaction rates and (ii) a diffusion-reaction-radiation (DRR) model to derive the densities of the Ar atoms in the various excited levels based on the rates obtained in the PIC/MCC simulation [47].

The aim of the present work is to extend both our prior experiments and simulations to gas mixtures containing small amounts of nitrogen. We consider the tight coupling of the kinetic particle simulation (PIC/MCC) and the radiation model (DRR) to represent a considerably more sophisticated approach as compared to models used in earlier studies of Ar/N_2 CCPs. Our approach has been experimentally validated based on measurements of the spatial distributions of the Ar $1s_5$ metastable atoms at various conditions [46] in Ar CCPs. This approach allows us to reliably compute the EEPF and to study its changes with the amount of N_2 added. Finally, our computational approach allows us to decouple and study separately the effect of the two mechanisms that are influenced by the nitrogen addition and that control the discharge behavior—the quenching of the Ar excited levels and the modification of the EEPF.

These effects of the N_2 admixture on the characteristics of a CCP are investigated, including the densities of the Ar metastable atoms as well as the intensities of the spectral lines belonging to the $2p \rightarrow 1s$ system of Ar. Below, in section 2 we describe our radio-frequency (RF) CCP experimental apparatus as well as the methods and equipments used for the optical measurements that include tunable diode laser absorption spectroscopy (TDLAS, for the measurements of the Ar $1s_5$ and $1s_3$ metastable atom densities) and OES (used for recording of emission of the Ar/N_2 plasma). Section 3 reviews the computational methods, while the experimental and computational results are presented and compared to each other in section 4. In section 5, a brief summary of the findings is presented.

2. Experimental setup and methods

The experimental system is the same as used earlier for measurements of the densities of Ar metastable atoms and the Ar-I spectral line intensities in a CCP operated in pure Ar gas, described in detail in [45]. To avoid repetition, the setup and the measurement methods are only briefly reviewed here.

The CCP discharge is ignited between two 14.2 cm-diameter flat disc stainless steel electrodes placed 4 cm apart, and situated inside a quartz cylinder. We use a 13.56 MHz Tokyo HY- Power RF-150 generator connected to the discharge cell via a Tokyo HY-Power MB-300 matching network, to sustain the plasma. The peak-to-peak value of the RF voltage is fixed at $V_{pp} = 300$ V. The experimental system is highly symmetric geometrically, which ensures that only a very small DC self-bias voltage develops, which is in the order of 1% of the applied voltage. This small voltage can safely be neglected in the modeling studies.

For pumping, a cascade of a turbomolecular and a rotary pump is used, establishing a base pressure of 3.4×10^{-5} Pa. The pressure (measured by a Pfeiffer CMR264 capacitive gauge) and the composition of the working gas is maintained by separate flow controllers for the two gases and with a precision needle valve at the vacuum side of the chamber. The total gas pressure and the N_2 content are varied within the ranges of 2.5–50 Pa and 0%–5%, respectively. The low base pressure, as well as a low leak-rate of the discharge cell (measured to be 1.2×10^{-5} sccm, by closing input and output valves of the chamber and monitoring the pressure rise over an interval of several days) are essential for investigating effects of small and controlled amounts of molecular admixtures on noble gas discharges. Considering the high ratio of the concentration of the added N_2 to that of the possible impurities, proper conditions for the measurements are confirmed.

For the (OES) intensity measurements, we use a Carl Zeiss Jena PGS-2 spectrometer equipped with a Peltier-cooled Greateyes ELSEs 2k512 BI UV3 detector. Light emitted from the central (approx. 1 cm-diameter) region of the plasma is captured with an optical fiber equipped with a collimator (type Thorlabs F220SMA-A) and oriented perpendicularly to the inter-electrode axis. Relative calibration wavelength-dependent sensitivity of the system is performed with an RS-15 Total Flux Calibration Light Source having a certified calibration report (that specifies the radiant flux of the lamp as a function of the wavelength in the range between 300 nm and 1100 nm) provided by Gamma Scientific. Using this approach, the intensity data do not represent absolute values.

Broadband spectra are also acquired by a low-resolution (Avantes AvaSpec-ULS2048L) spectrometer. Exemplary measured OES results for pure Ar and 95% Ar + 5% N_2 mixture at 20 Pa pressure and 300 V_{pp} voltage are shown in figure 1. The part of the wavelength domain used in the OES measurements is marked with yellow background. The spectral lines considered in this work are listed in table 1. For these lines, intensity data are shown in units proportional to the incident radiant flux, in accordance with the computed intensities,

$$I_{ij} = n_i A_{i,j} \eta_{ij}, \tag{1}$$

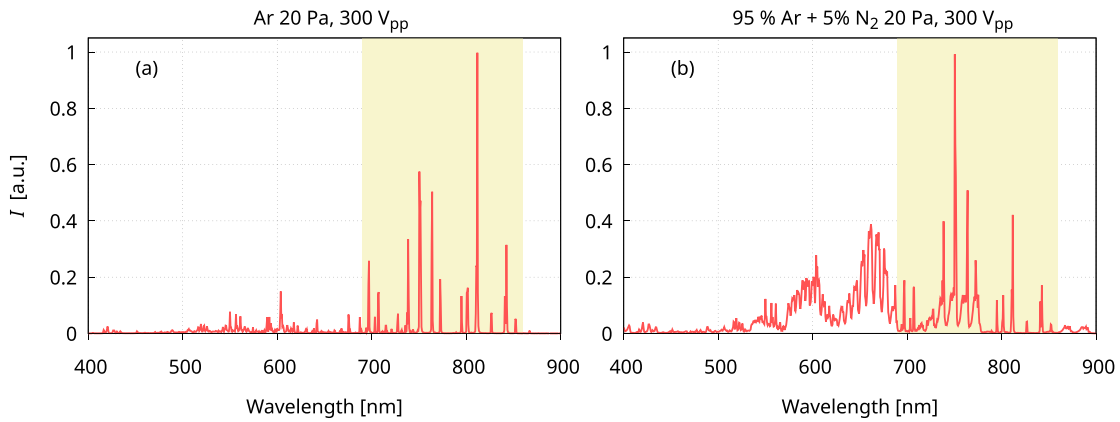


Figure 1. Exemplary spectra recorded with the low-resolution (AvaSpec-ULS2048L) spectrometer: (a) pure Ar, (b) 95% Ar + 5% N_2, at 300 V peak-to-peak RF voltage and 20 Pa pressure. The yellow shaded regions mark the wavelength domain where the intensities of the Ar 2p→ 1s spectral lines are investigated. The recording was made at the midplane of the discharge.

Table 1. Wavelength (in air) and the corresponding transition of the Ar-I lines investigated. Lines marked with * are used in the laser absorption measurements. These lines are not resolved in the OES measurements, however, even with the higher-resolution spectrometer (PGS-2) used.

Wavelength [nm]	Transition
696.543	$2p_2 \rightarrow 1s_5$
706.722	$2p_3 \rightarrow 1s_5$
714.704	$2p_4 \rightarrow 1s_5$
727.294	$2p_2 \rightarrow 1s_4$
738.398	$2p_3 \rightarrow 1s_4$
751.465	$2p_5 \rightarrow 1s_4$
750.387	$2p_1 \rightarrow 1s_2$
763.511	$2p_6 \rightarrow 1s_5$
772.376*	$2p_7 \rightarrow 1s_5$
772.421*	$2p_2 \rightarrow 1s_3$
800.616	$2p_6 \rightarrow 1s_4$
801.479	$2p_8 \rightarrow 1s_5$
810.369	$2p_7 \rightarrow 1s_4$
811.531	$2p_9 \rightarrow 1s_5$
826.452	$2p_2 \rightarrow 1s_2$
840.821	$2p_3 \rightarrow 1s_2$
842.465	$2p_8 \rightarrow 1s_4$
852.144	$2p_4 \rightarrow 1s_2$

where the indices i and j correspond to the upper and lower levels of the transitions, respectively, A_{ij} are the Einstein coefficients for the $i \rightarrow j$ transition, and n stands for the density. The coefficient η_{ij} is the escape factor for the given transition, and will be discussed in section 3.

Identification of the Ar lines of interest is rather straightforward for the case of pure Ar discharges; the resolution of the PGS-2 spectrometer allows easy separation of two pairs of prominent lines (750.387 nm, 751.465 nm) and (810.369 nm and 811.531 nm). Since the (772.376 nm, 772.421 nm) pair of lines is, however, not resolved, values communicated for the intensities represent the added intensities of these two lines.

Emission from excited N_2 molecules is not used in this work for the characterization of the plasma. In the presence of a nitrogen admixture, however, molecular emission bands (first positive system of N_2) overlap with the 2p→ 1s system of Ar-I lines, as seen in figure 1(b). To extract the intensities of Ar lines, the following algorithm was applied. First, all data points within 0.3 nm of the expected Ar peaks (see table 1) were masked out of the measured Ar/N_2 spectrum. Then, a spectrum obtained in pure N_2 using the same applied voltage and a pressure as close as available to the N_2 partial pressure in the original Ar/N_2 mix was selected. This pure N_2 spectrum was multiplied by a scaling factor to match the remaining N_2 signal in the masked Ar/N_2 spectrum. Here, least absolute deviations rather than least squares fitting was used, to mitigate the contribution of potentially unmasked, low-intensity outlying Ar peaks.

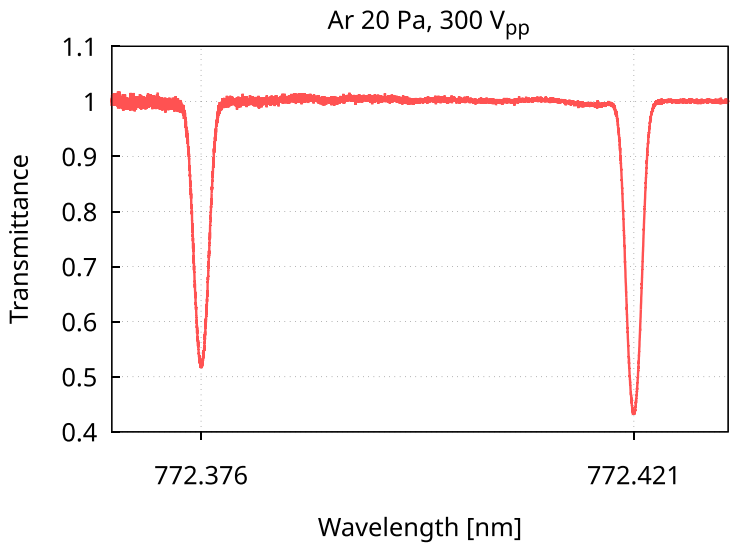


Figure 2. Exemplary TDLAS transmittance spectrum at 300 V peak-to-peak RF voltage and 20 Pa pressure in pure Ar. The wavelength range covers both absorption lines at 772.376 and 772.421 nm. The recording was made at the midplane of the discharge.

A single, wavelength-independent, correction factor was sufficient to fit the data adequately in all experimental conditions. This procedure provided a fitted N_2 baseline that could finally be subtracted from the original Ar/N_2 spectrum, leaving the isolated Ar peaks to be extracted.

The Ar $1s_5$ and $1s_3$ metastable atom densities and the gas temperature are determined using TDLAS. We measure the absorption on the $Ar(1s_5 \rightarrow 2p_6)$ transition at a wavelength of 772.376 nm and on the $Ar(1s_3 \rightarrow 2p_2)$ transition at wavelength of 772.421 nm using a Toptica LD-0773-0075-DFB-1 system driven by a control unit Toptica DLC DFB PRO L. The laser light passes through the plasma along its diameter at the mid position of the electrode gap and is detected at the other side of the chamber by a photodiode. To perform proper background subtraction, detector signals were recorded with and without discharge, both with laser on and off states. Assuming dominating Doppler broadening, the amplitude of the absorption provides information about the line-integrated metastable atom density, while the width of the line conveys information about the gas temperature. For more details see, e.g. [46]. Figure 2 shows exemplary absorption line profiles for pure Ar at 300 V peak-to-peak RF voltage and 20 Pa pressure.

3. Computational method

Below, we briefly review our one-dimensional hybrid computational framework, which was developed for CCPs operated in pure Ar gas, for the self-consistent calculation of the densities of atoms in excited levels and the intensities of selected Ar-I spectral lines [46, 47]. Afterwards, the extensions for N_2-containing plasmas will be described.

3.1. Previous model for pure Ar discharges

The approach was based on the coupling of (i) a PIC/MCCs code that included Ar atoms in numerous excited levels in addition to the ground-state Ar atoms as targets for electron-impact collisions, and (ii) a DRR code that solved the diffusion equations of Ar atoms in the excited levels, considering all their sources and losses, including electron-impact and radiative transitions between the various levels as well as quenching processes and pooling ionization. Obtaining the solution required execution of the two codes iteratively.

The PIC/MCC simulations were one-dimensional in space and three-dimensional in velocity space. The calculations used a set of 30 excited levels listed in [48], which work provides a comprehensive set of cross sections for electron-impact collisions: the elastic momentum transfer collision, 31 excitation and the ionization cross section of ground state Ar atoms, as well as 435 stepwise excitation processes among excited levels. These cross section data were adopted from the BSR [49, 50] database [51] of LxCat [52, 53]. For all the excitation channels, the corresponding reverse reactions, i.e. superelastic collisions, were also considered in [46, 47]. Stepwise ionization from the 1s and 2p levels was accounted for

Table 2. Collision processes of Ar^+ and N_2^+ ions included in the model.

Process	Type
$Ar^+ + Ar \rightarrow Ar^+ + Ar$	isotropic
$Ar^+ + Ar \rightarrow Ar + Ar^+$	charge exchange
$Ar^+ + N_2 \rightarrow Ar^+ + N_2$	isotropic (Langevin)
$Ar^+ + N_2 \rightarrow Ar + N_2^+$	charge transfer
$N_2^+ + N_2 \rightarrow N_2^+ + N_2$	isotropic
$N_2^+ + N_2 \rightarrow N_2 + N_2^+$	charge transfer
$N_2^+ + Ar \rightarrow N_2^+ + Ar$	isotropic (Langevin)
$N_2^+ + Ar \rightarrow N_2 + Ar^+$	charge transfer

by using the cross sections provided in [54] and we adopted the rate of pooling ionization due to collisions between atoms in the 1s levels from [55]. For the Ar^+ ions, we followed the approach of [56] and considered an elastic differential collision cross section partitioned into isotropic and backward (charge exchange) components, which are related to the momentum transfer cross section as

$$\sigma_{\mathrm{mom}}(\varepsilon) = \sigma_{\mathrm{iso}}(\varepsilon) + 2\sigma_{\mathrm{back}}(\varepsilon). \tag{2}$$

The DRR model was based on the diffusion equations for the 30 excited Ar level populations [57], which were solved using the finite difference forward-time-centered-space method [57, 58], with a boundary condition that accounts for the possible reflection of the species at the electrode surfaces (for more details see [47]). Besides the electron-impact collisions, 143 radiative transitions were also included in the model, as in [59]. For all of these transitions, the partial re-absorption of the radiation was accounted for by using an escape factor appropriate for a slab geometry, see [60, 61]. Additionally, the DRR code included quenching reactions as well: for the metastable atoms both 2-body and 3-body quenching reactions [62], for the 2p excited levels 2-body reactions by neutrals [63, 64] were considered. Inelastic processes due to ion impact were not considered for the following reason. Due to comparable masses of the projectile and target species, only about half of the kinetic energy in the laboratory system is available for the inelastic process. Together with the inefficient conversion of this energy into excitations of the electronic shell makes these types of collisions negligible in most cases except maybe in some special conditions and then only in the high-voltage sheath region near the electrodes.

Radial diffusion losses for the excited species were taken into account by adopting a radial loss frequency corresponding to the chamber radius. Having obtained a converged solution for the excited Ar atom densities, the light emission from the plasma was calculated via equation (1), by adopting the escape factor from [65] for cylindrical geometry, allowing comparison with experimental spectrally resolved light emission collected in a direction perpendicular to the discharge axis [47]. The computational results for the spatial density distributions of the $1s_5$ metastable Ar atoms were successfully benchmarked with experimental data obtained from TDLAS measurements [46].

For more details on the computational framework for Ar discharges the reader is referred to [46, 47].

3.2. Extension of the model to N_2-containing discharges

The computations presented in this work are based on the modeling approach outlined above. Adapting this model to the case of Ar–N_2 plasmas requires extensions of both the PIC/MCC and DRR codes. In the PIC/MCC code, N_2 molecules appear as additional targets for electron-impact collisions, for these collisions we adopt the cross section set from [66, 67]. This set includes the elastic momentum transfer cross section, as well as cross sections for a number of vibrational and electronically excited levels, and ionization. For the N_2^+ ions created in the latter process and for Ar^+ ions, the collision processes listed in table 2 are considered.

For the ion-neutral interactions we consider elastic collisions only. For the 'symmetric' processes, i.e. $Ar^+ + Ar$ and $N_2^+ + N_2$ collisions we follow the approach of [56] already introduced above, in the review of the model of pure Ar discharges (i.e. we approximate the differential cross section as the sum of an isotropic component and a backward scattering part). For the $N_2^+ + N_2$ collisions, we take the data from [68]. In this work, the symmetric charge transfer cross section is given only from about 3 eV energy. We extend this cross section to lower energies using the constraints that the momentum transfer cross section, $\sigma_{\mathrm{mom}}(\varepsilon)$, should approach the Langevin cross section in the limit of low ion energy and that equation (2) holds. In the case of 'asymmetric' processes, i.e. $Ar^+ + N_2$ and $N_2^+ + Ar$ we consider elastic collisions both without and with electron transfer. For the first case, we calculate the Langevin cross section of the process (based on polarizibilities from [69]) and assume isotropic scattering in the

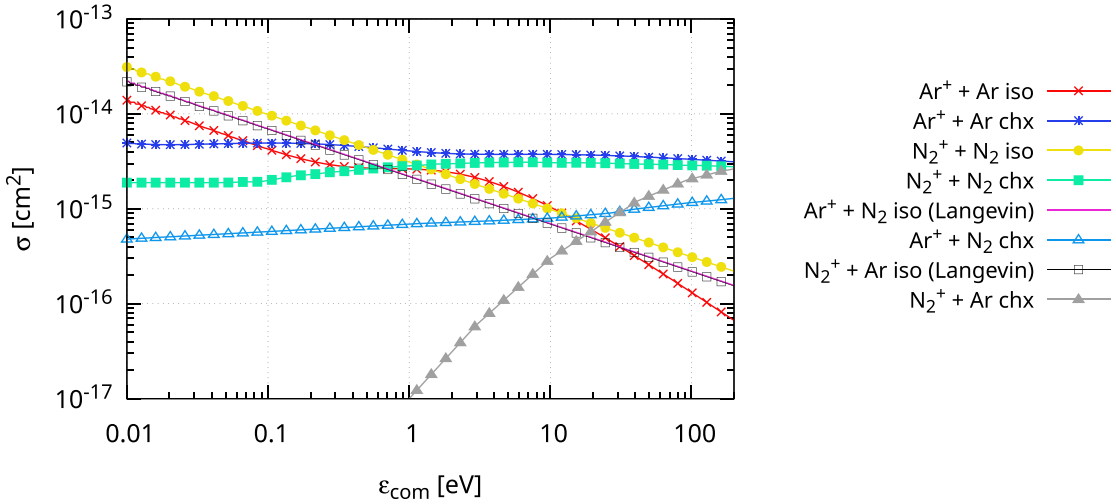


Figure 3. Cross sections for isotropic (iso), charge-exchange (chx) scattering of Ar^+ and N_2^+ ions as a function of the center of mass energy, ε_{com}. Note that the Langevin cross sections for the $Ar^+ + N_2$ and $N_2^+ + Ar$ collisions are indistinguishable in this plot as the reduced mass is the same for the two cases and the polarizibilities of Ar atoms and N_2 molecules are nearly the same [69].

collision. For the charge transfer reactions, our estimates of the cross sections are based on [70, 71]. The cross sections for the ion–neutral collisions are depicted in figure 3, as a function of the center-of-mass energy, $\varepsilon_{com} = \mu_r g^2/2$, where μ_r and g are, respectively, the reduced mass and the relative velocity of the collision partners (the projectile and the target). The velocity of the target is sampled from a Maxwell–Boltzmann distribution corresponding to T_g, every time when a collision probability has to be evaluated.

In the DRR part of the model, quenching reactions of N_2 molecules with Ar 1s metastable and resonant atoms are incorporated with rate coefficients adopted from [72]. The rest of the computation proceeds like in the case of pure Ar discharges, except that a *local* escape factor is now used in the DRR part, meaning that self-absorption is computed as a function of the spatial coordinate [61]. No calculations for the densities of excited species of nitrogen are targeted and no emission features of N_2 and N_2^+ molecules are included in the model.

The PIC/MCC simulation is conducted with a uniform spatial grid with $N_g = 600$ points and one RF cycle is split into $N_t = 2000$ to 12 500 time steps. For the ions, subcycling is used with a time step of $\Delta t_i = 20\Delta t_e$. With these settings, the stability and accuracy criteria of the PIC/MCC scheme [73, 74] are fulfilled. We include ion-induced electron emission at the electrodes with an effective yield of $\gamma = 0.07$ and the elastic reflection of electrons at the electrodes with a probability of $r = 0.7$. These values were found to result in the best agreement between measured and computed discharge characteristics in a multi-diagnostics benchmarking study at similar conditions [75].

The PIC/MCC code computes and stores the rates of all electron-impact processes, which are subsequently used as input for the DRR model. In turn, the density distributions of the excited Ar atoms are used during the next call of the PIC/MCC module. This iteration proceeds, to reach convergence, for typically few times 10^4 RF cycles. The calculations are carried out assuming a gas temperature of T_g = 300 K, in accordance with the experiments that found only a marginal increase of the gas temperature with respect to ambient temperature.

Finally, we note that the present model was developed to study the effect of small amounts of N_2 admixtures on Ar discharges and it was not the aim to account for all the processes, e.g. N_2 vibrational kinetics, which are essential for the description of discharges with a high N_2 content. Extension of the model for high-N_2-content and pure N_2 discharges remains future work, as well as the computation of the emission from N_2 molecular bands.

4. Results

In this section, we present the comparison between the measured and the computed metastable atom densities and spectral line intensities, and discuss additional computational results for the discharge characteristics as well, including spatial distributions of the charged particle and excited Ar atom densities, and the electron energy distribution function. The results are presented for $0 \leqslant [N_2] \leqslant 5\,\%$

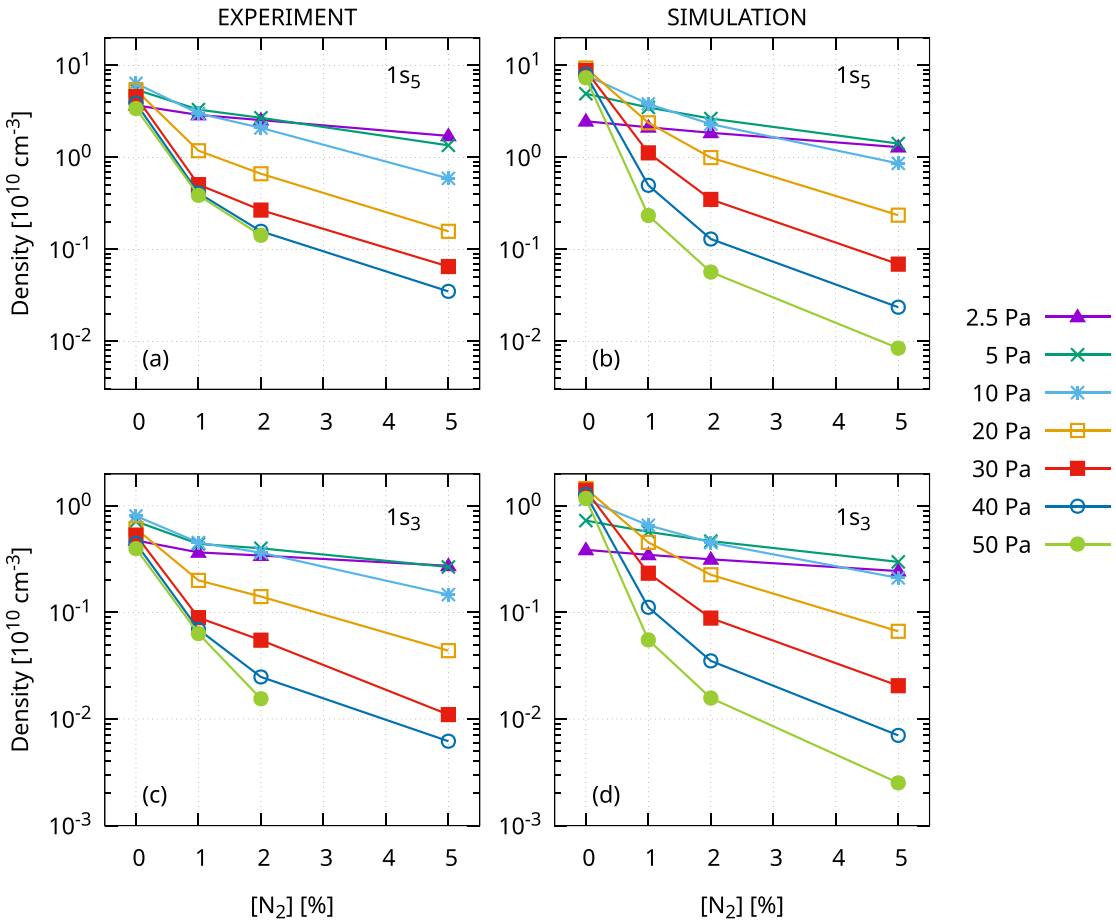


Figure 4. Comparison of the measured (left column) and computed (right column) densities of Ar metastable species as a function of the N_2 admixture concentration, at various gas pressures, at the center of the discharge. Note, that the density scale differs for the $1s_5$ and $1s_3$ species.

nitrogen admixture concentration, $2.5 \leqslant p \leqslant 50$ Pa (total) gas pressure, and a fixed peak-to-peak RF (f = 13.56 MHz) voltage of V_{pp} = 300 V.

Figure 4 shows the measured and computed densities of the Ar $1s_5$ and $1s_3$ metastable atoms in the middle of the electrode gap, as a function of nitrogen admixture concentration and gas pressure. The experimental and modeling results are in fair agreement over the whole range of parameters, with somewhat (up to a factor of approximately two) higher computed values as compared to the experimental data. These differences may be explained by the fact that the model assumes a one-dimensional geometry, and disregards thereby most of the radial effects that are present in the experiment. In the latter, the excited atom densities are expected to decay towards the cylindrical (quartz) wall that confines the plasma. For this reason, the line-averaged experimental values are expected to be lower than the values on the central axis provided by the simulations. Note, however, that for 2.5 and 50 Pa this appears not to be the case, hinting to possible hollow profiles of the metastables at these conditions.

The experimental and computed data sets, for both metastable species, show a decrease of the density (at the discharge center) as a function of the nitrogen content, $[N_2]$. This decay becomes progressively faster when the pressure is increased: at the lowest pressure of 2.5 Pa, $[N_2] = 0 \rightarrow 5\%$ results in a density decay of about a factor of two, whereas at the highest pressure of 50 Pa, the same amount of nitrogen suppresses the metastable atom density by up to three orders of magnitude. Note, that at 50 Pa pressure no experimental data are shown above $[N_2] = 2\%$ because the metastable atom densities decayed below the detection limit.

Beside the metastable atom densities, the presence of a small N_2 admixture has a strong effect on the plasma composition as well, as illustrated in figure 5. In the case of discharges in pure Ar, the density of Ar $1s_5$ atoms is typically one order of magnitude larger as compared to the electron and Ar^+ density. At low pressure, the Ar $1s_5$ density profile peaks at the middle of the electrode gap. With increasing pressure, however, a dip develops at the center as the positions of the maximum values of the density are correlated with the positions of the production of Ar $1s_5$ atoms, which occur near the sheath edges.

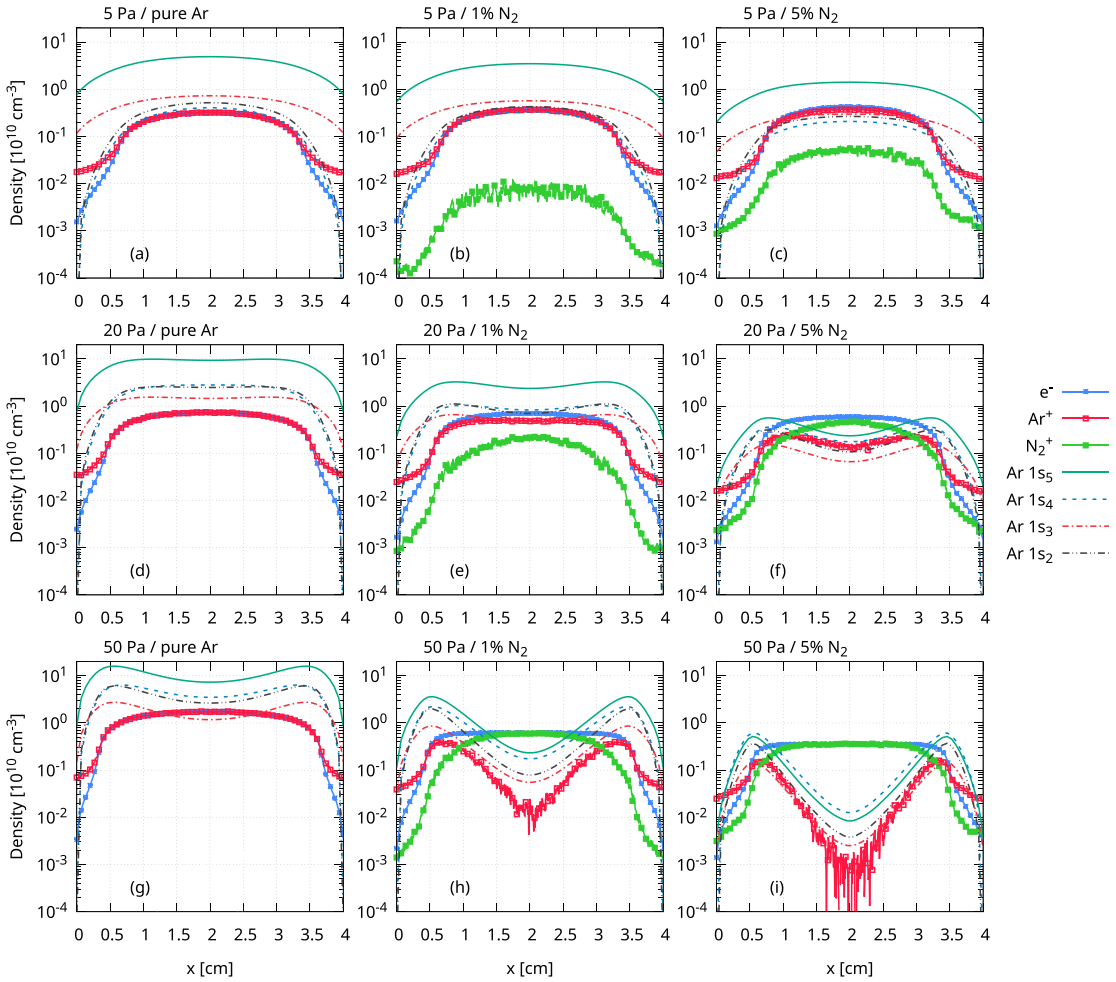


Figure 5. Density distributions of charged particles and Ar 1s excited species at various N_2 contents and gas pressures. V_{pp} = 300 V. The powered electrode is situated at $x = 0$ cm, while the grounded electrode is at $x = 4$ cm.

This correlation is ensured by the high collisional losses of Ar $1s_5$ atoms which makes the contribution of transport (diffusion) negligible and thus ensures local balance for their density. The Ar $1s_3$ atoms are governed by equivalent processes and their density distribution is thus similar to that of the Ar $1s_5$ atoms, but it typically has an order of magnitude lower value. The densities of the Ar atoms in the resonant $1s_4$ and $1s_2$ levels also follow similar distributions, but with more significant density drop in the vicinity of the electrodes, a consequence of the lower imprisonment of the resonant radiation from these levels. The moderate spatial decays observed for the Ar atoms in the metastable levels can be explained by their partial reflection at the boundaries. At 50 Pa, the density ratios of the atoms in the 1s excited levels (which copy the ratios of the respective statistical weights) indicate a strong 'mixing' of the excited levels by electron-impact collisions, as found also in [3].

Adding 1% N_2 to Ar, at the low pressure of 5 Pa (conditions for figure 5(b)), causes minimum changes to the density profiles of the electrons, Ar^+ ions, and Ar atoms in the 1s levels. The only notable effect is the appearance of N_2^+ ions, with a few percent density as compared to Ar^+ ions. At the higher N_2 content of 5%, a significant increase of the N_2^+ ion density is observed as well as a decay of the Ar 1s level populations, as seen in figure 5(c). At increased gas pressure, all these changes become more pronounced: for the same $[N_2]$, we observe a gradually stronger build-up of the N_2^+ and a decay of Ar^+ population and a more marked decay of the Ar excited level populations. Due to the prominence of the quenching of Ar 1s levels by N_2 molecules, the 1s level populations become only significant at the sheath edge regions at high p and nitrogen concentration (figure 5(i)). The formation of a 'dip' in the profile of the Ar^+ ions at higher pressures and N_2 concentrations point to the presence of volumetric losses of these species that exceed their production (by ionisation). The only reaction in the simulations is the conversion into N_2^+ ions via charge exchange. Due to the small but not negligible difference in the ionisation energies (15.76 eV for Ar and 15.58 for N_2), the reverse process is strongly suppressed. Consequently, N_2^+ ions amass in the center of the discharge, replacing almost entirely the Ar^+ ions there.

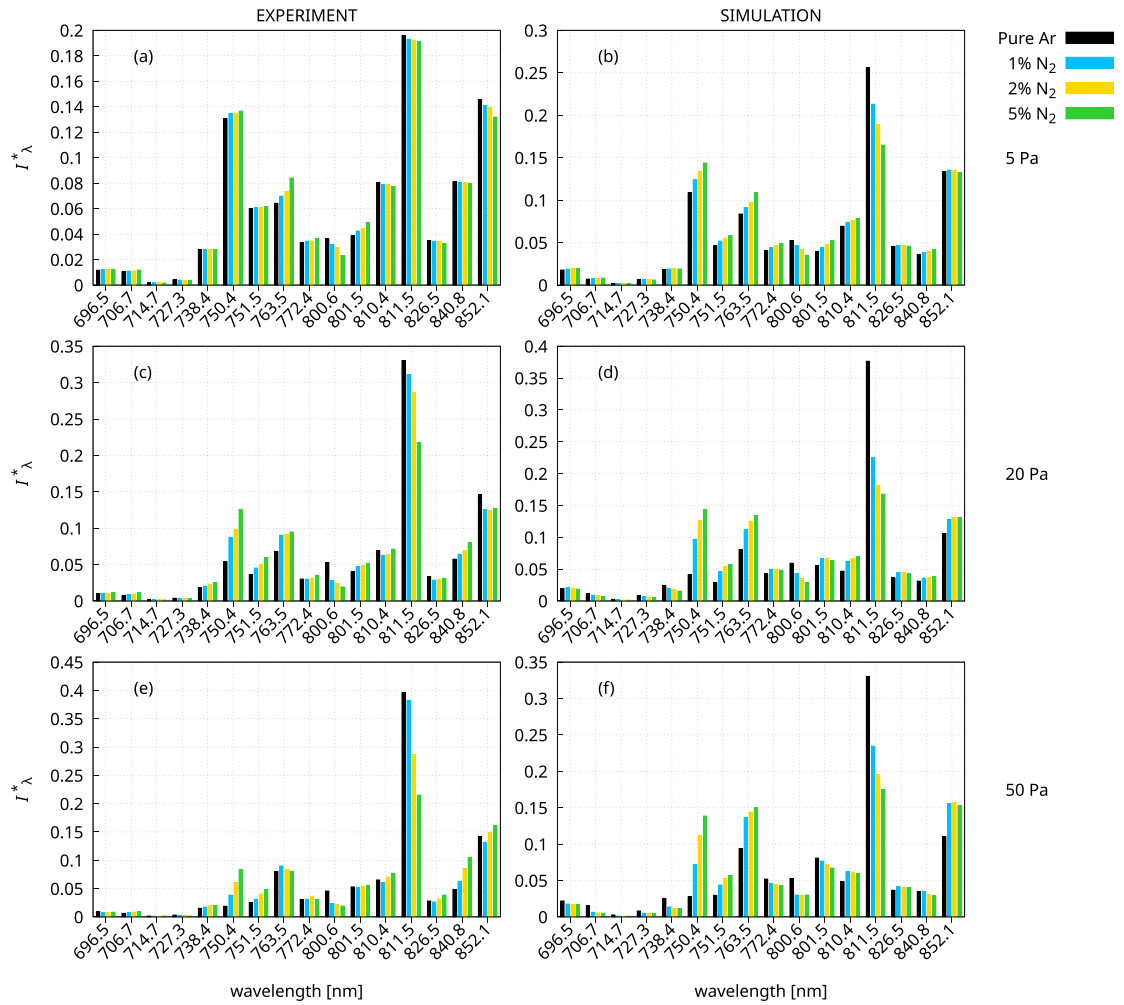


Figure 6. Measured (left) and computed (right) intensities of Ar 2p→1s spectral lines at the center of the discharge, for various pressures and nitrogen contents. The intensity values are normalized as $\sum I^*_\lambda = 1$, for each set of conditions, both for the experimental and computational results.

Before the presentation of the spectral line intensities, we recall that only *relative intensity calibration* of the OES setup was carried out in our experiments (see section 2). Therefore, we do not have access to the absolute intensities of the spectral lines in the experiment. We can, nonetheless, (i) compare the experimental and simulation results to each other for the same set of conditions by presenting normalized line intensities, and (ii) reveal the real trends of line intensities by comparing experimental (or simulation) results obtained at varying discharge conditions (e.g. as a function of the N_2 concentration). In the first case, the normalized intensities will be denoted as I^*_λ, for which $\sum I^*_\lambda = 1$ holds, both for the experimental and computational data, while in the second case the intensity values will be denoted as I_λ. We note that the presentation of normalized line intensities could be considered a generalization of the line ratio method [9–16] that monitors the relative changes of the intensities of two spectral lines, to a bigger number of lines. This presentation also preserves the ratio between any two lines in the same spectrum. (Data presented this way are meaningful only when a fixed set of lines is used.)

Normalized I^*_λ intensities of the selected set of Ar 2p→ 1s spectral lines, listed in table 1, measured in the experiments and derived from the modeling calculations are displayed in figure 6, for various pressures and nitrogen contents in the discharge gas. For an easier observation of the effects for lower-intensity spectral lines, the same data are also reproduced in figure 7 using a logarithmic intensity scale.

The general trends between the data sets match for all conditions, although the simulations predict somewhat more drastic changes as a consequence of the presence of N_2 on some of the spectral line intensities, as compared to the experiments. Individual lines 'respond' in various ways to the presence of N_2. Taking as an example the case of the intermediate pressure of 20 Pa, we observe, e.g. a growth of the (normalized) intensity of the 750.4 nm line, a decrease of the intensity of the 811.5 nm line, while the intensities of some of the lines (e.g. the 826.5 nm line) hardly change as a function of $[N_2]$.

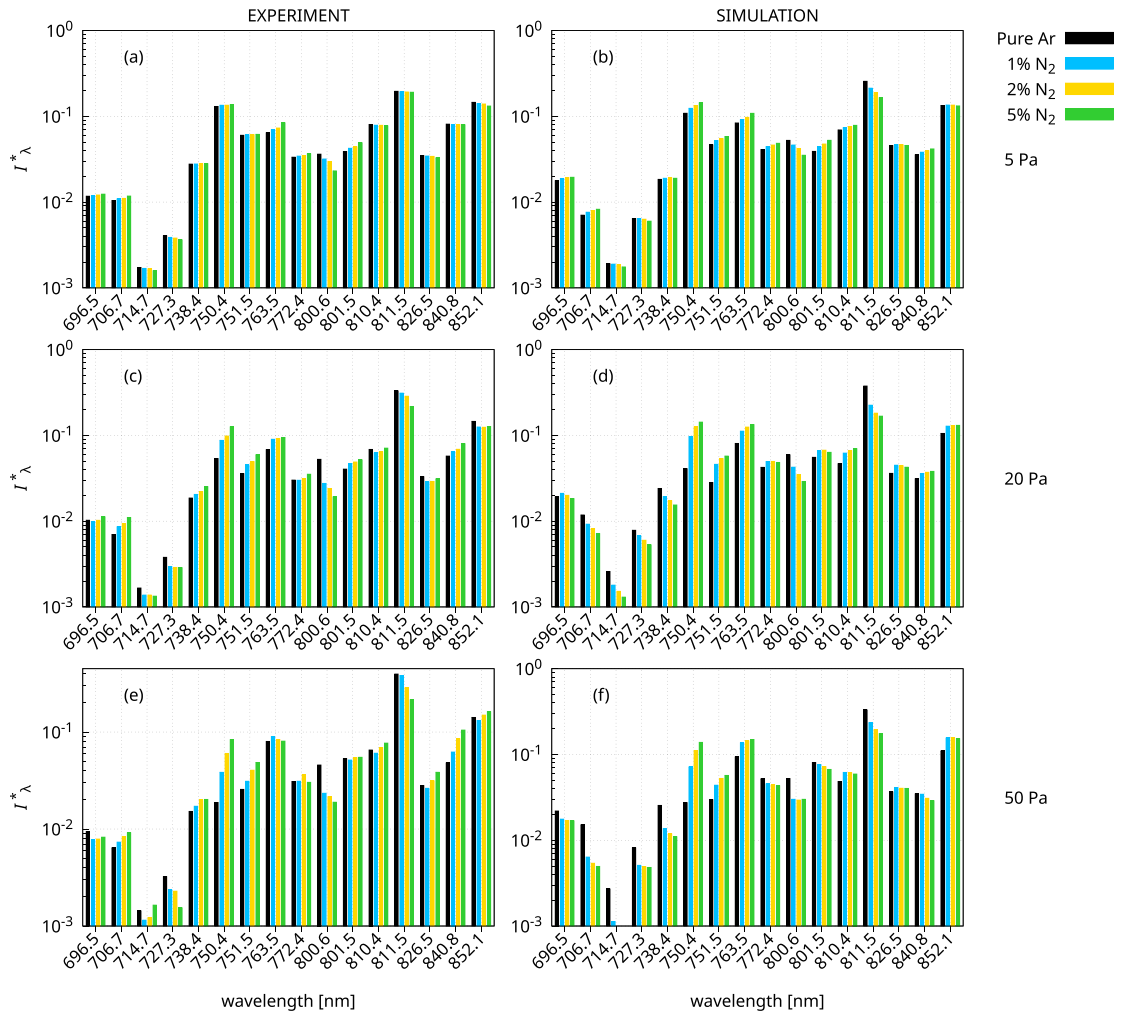


Figure 7. Same as in figure 6, but with a logarithmic scale for the normalized intensity.

These specific behaviors originate from the different populating mechanisms of the upper levels of these transitions and the varying degrees of sensitivity on the presence of the nitrogen admixture. Our observations are consistent with those presented in [1] for DC discharges. The latter fact suggests that the strong temporal modulation of the EEPF and the significant spatial gradients present in a CCP discharge do not affect significantly the underlying mechanisms of atom excitation.

The presentation of the spectral line intensities in relative units hides the influence of N_2 content in the working gas on the *real* intensities. To reveal the real behavior, the spectral line intensities are re-plotted in figure 8, where the data in each of the panels allow comparison between the data corresponding to various N_2 concentrations. This figure reveals that for all the lines and at all pressures, the intensity always decreases as the nitrogen content is increased. This experimental observation is correctly reproduced by the numerical results. The decrease in intensity is relatively modest (a factor of few) at the low pressure of 5 Pa (figures 8(a),(b)) but becomes rather drastic as the pressure is increased. For most of the lines at the high pressure of 50 Pa, intensity lowers by 1–2 orders of magnitude even for an N_2 concentration as low as 1%.

The effect of the N_2 content on the densities of the Ar atoms in the 1s and 2p levels in the CCP operated at $V_{pp} = 300$ V is depicted in figures 9 and 10, respectively. These data were taken at the center of the discharge. For the 1s levels, the data (with their spatial distributions) were already shown in figure 5, but figure 9 allows a clearer view of the effect of the nitrogen content. The latter results in a depletion of all 1s levels at all the pressures covered in the figure. The factor-of-few depletion at the lowest pressure reaches three orders of magnitude at the highest pressure of 50 Pa, for the $1s_5$ level. This decay contributes significantly to the suppression of the intensities of the spectral lines emitted by levels excited preferentially by stepwise electron impact, like the 811.5 nm line (see figure 8(f)).

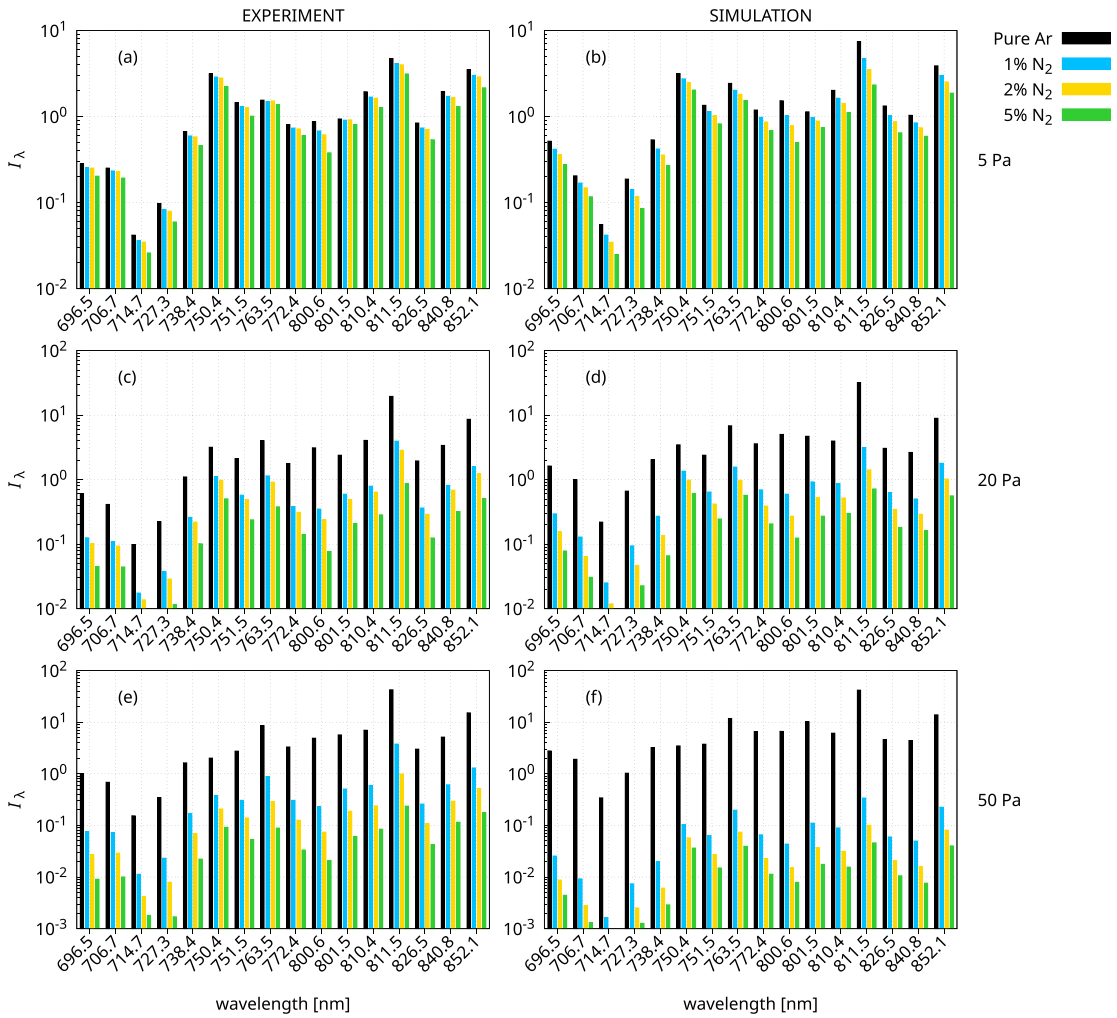


Figure 8. Measured (left) and computed (right) intensities of Ar 2p→1s spectral lines at the center of the discharge, for various pressures and nitrogen contents. Here, the spectral line intensities are given in arbitrary units, but in each of the panels the intensities corresponding to various nitrogen contents can be compared quantitatively.

For the 2p level populations, shown in figure 10, we observe quite different rates of depletion. At the lowest pressure, the $2p_1$ and $2p_9$ levels can be mentioned as examples of the weakly and strongly influenced ones, respectively, in the presence of N_2 admixture. This difference, as already pointed out in previous works (e.g. [1]), originates in the leading populating mechanisms of these two levels: the former ($2p_1$) is dominantly populated from the ground state, while the latter ($2p_9$) is dominantly populated by stepwise excitation from the 1s levels by electron impact. With increasing pressure, the effect of N_2 becomes much more pronounced, reaching an extreme depletion of the $2p_9$ level population at $[N_2] = 5\%$.

The pronounced depletion of the 1s levels results in a strong overall suppression of the stepwise excitation processes of Ar 2p levels, in general. This is illustrated in figure 11, which shows the direct and stepwise excitation rates (with the latter resolved for the four 1s levels) for selected 2p levels, $2p_1$, $2p_2$, and $2p_9$, for pressures of 5 Pa and 50 Pa, and N_2 concentrations of 0% and 5%. These three representative levels were chosen to illustrate the changes because they are typically affected in different proportion by direct and step-wise excitation: $2p_1$ is predominantly produced by direct excitation from the ground state (figures 11(a) and (g)), $2p_2$ is produced from the ground state at low pressures (figure 11(b)) and from the 1s levels at elevated pressures (figure 11(h)), while $2p_9$ is always determined by step-wise excitation, through $1s_5$ in particular (figures 11(c) and (i)), in pure Ar discharges.

The presence of nitrogen modifies the excitation rates only slightly at the lower pressure of 5 Pa, the importance of direct and stepwise excitation is 'switched' only for the $1s_5 \rightarrow 2p_9$ channel. At 50 Pa pressure, however, substantial changes take place as a response to N_2 addition to the gas. Most importantly, all stepwise excitation channels are substantially suppressed and the direct excitations becomes the leading process. As this process requires high-energy electrons, the profiles acquire a double-peaked

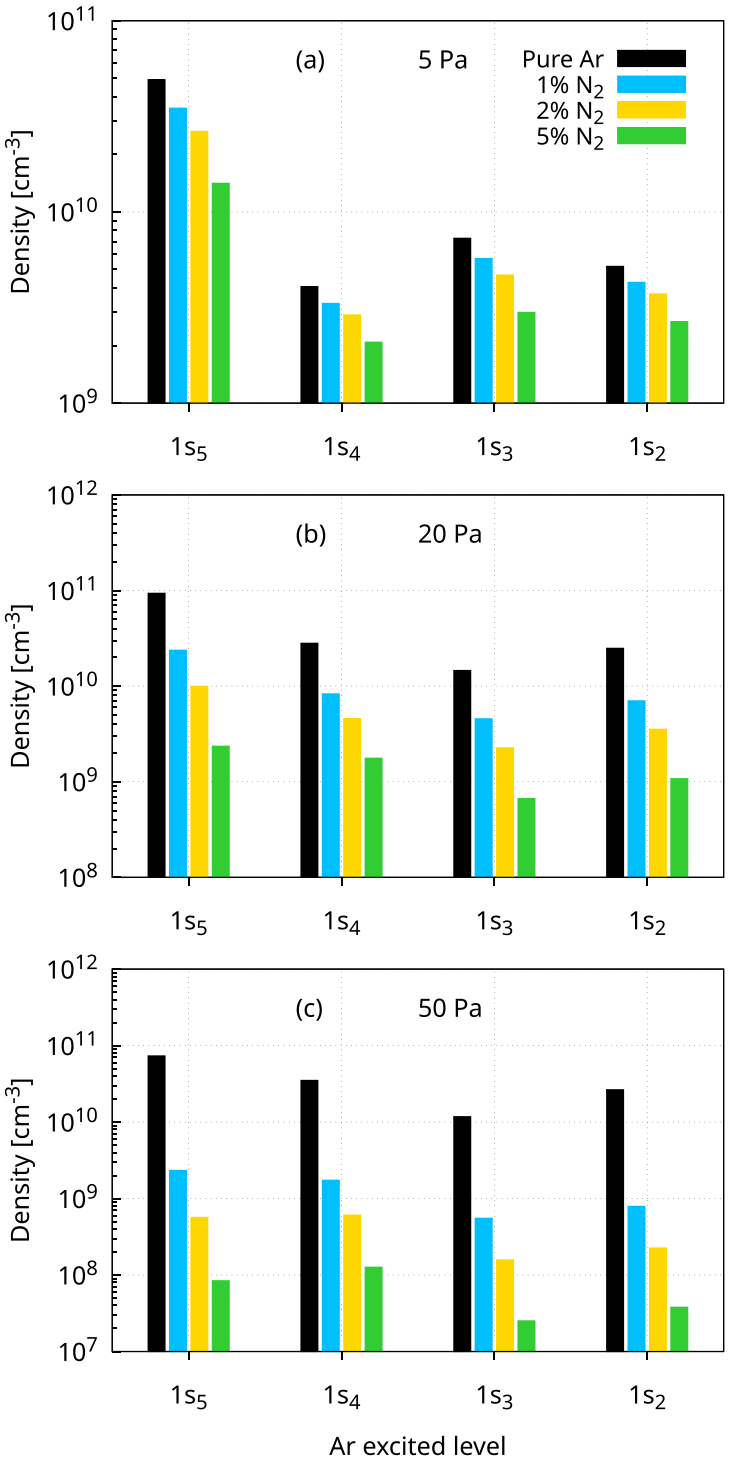


Figure 9. Computed populations of the Ar 1s excited levels as a function of N_2 content, for (a) $p = 5$ Pa, (b) 20 Pa, and (c) 50 Pa, at the center of the discharge.

shape as high-energy electrons can predominantly be found near the sheath boundaries at this high pressure. While stepwise excitation requires lower electron energy, the stepwise excitation rates also develop holes at the discharge center because of the depleted density of the Ar atoms in the 1s levels under such conditions, which is the result of their quenching by N_2 molecules. The opposite changes of the relative intensities of the spectral lines (shown in figure 6) originating from the $2p_1$ level (e.g. at 750.6 nm) vs. from the $2p_9$ level (e.g. at 811.5 nm) can be explained by the mechanisms discussed above. The population mechanisms of the $2p_2$ level represent an intermediate case between those acting for the $2p_1$ and $2p_9$ levels and this explains the lower sensitivity of the relative intensities of the spectral lines originating from $2p_2$ as a function of $[N_2]$.

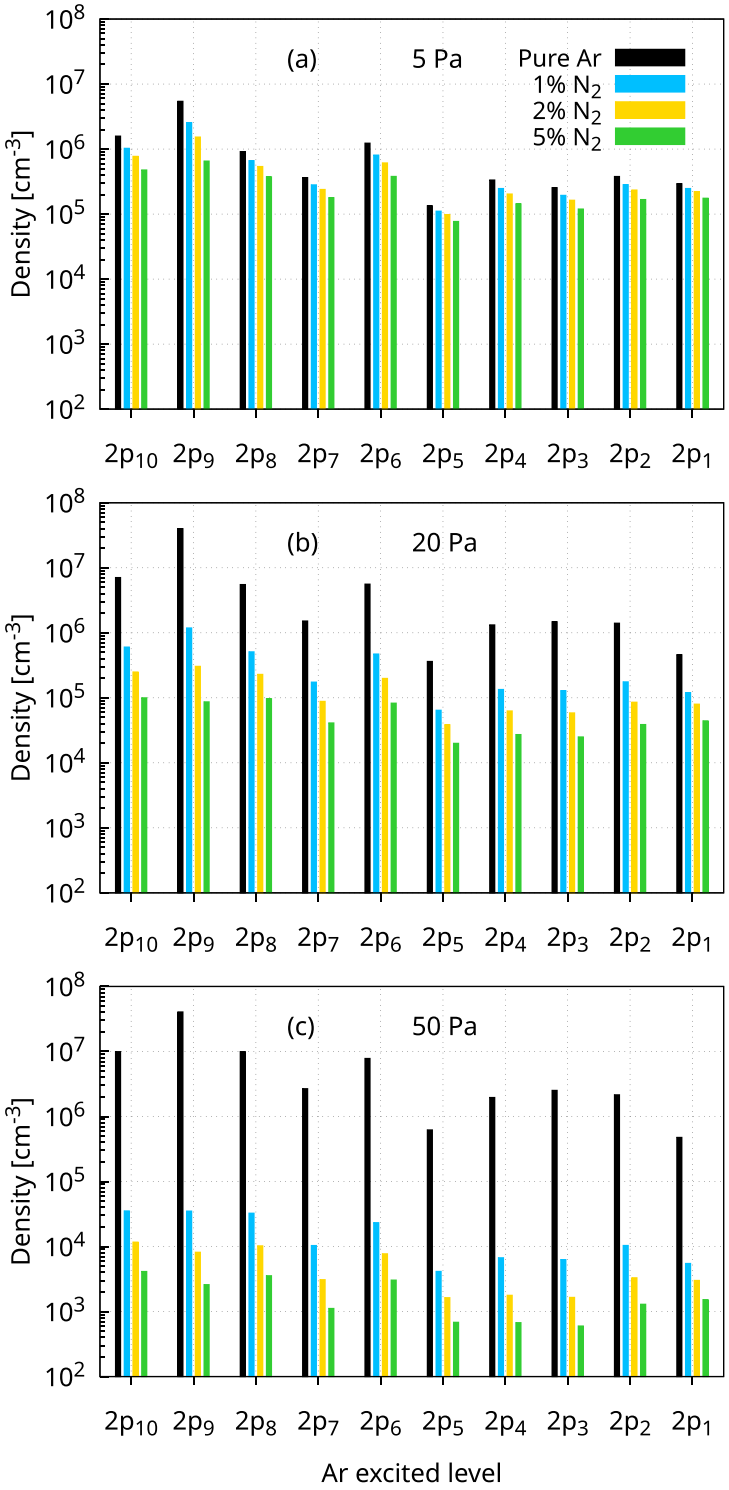


Figure 10. Computed populations of the Ar 2p excited levels as a function of N_2 content, for (a) $p = 5$ Pa, (b) 20 Pa, and (c) 50 Pa, at the center of the discharge.

As already discussed in section 1, N_2 has two major effects on the excited level kinetics: (i) it changes the EEPF and (ii) it quenches the excited Ar levels. These two effects can be separated in the simulations by turning on or off the quenching processes. Figure 12 shows the Ar-I spectral line intensities for pure Ar discharges and for Ar/N_2 discharges with $[N_2] = 5\%$, both in the presence and absence of the quenching processes in the simulations. At 5 Pa, the changes of the relative intensities are modest. For the lines of which the intensities appear to be sensitive to the presence of N_2, both effects seem to have an influence. This situation changes towards higher pressures. At 50 Pa, the quenching process seems to have a very strong effect in the case of some of the lines: the relative intensity decreases strongly for the 811.5 nm line (originating from the $2p_9$ level) and increases strongly for the 750.4 nm line (originating

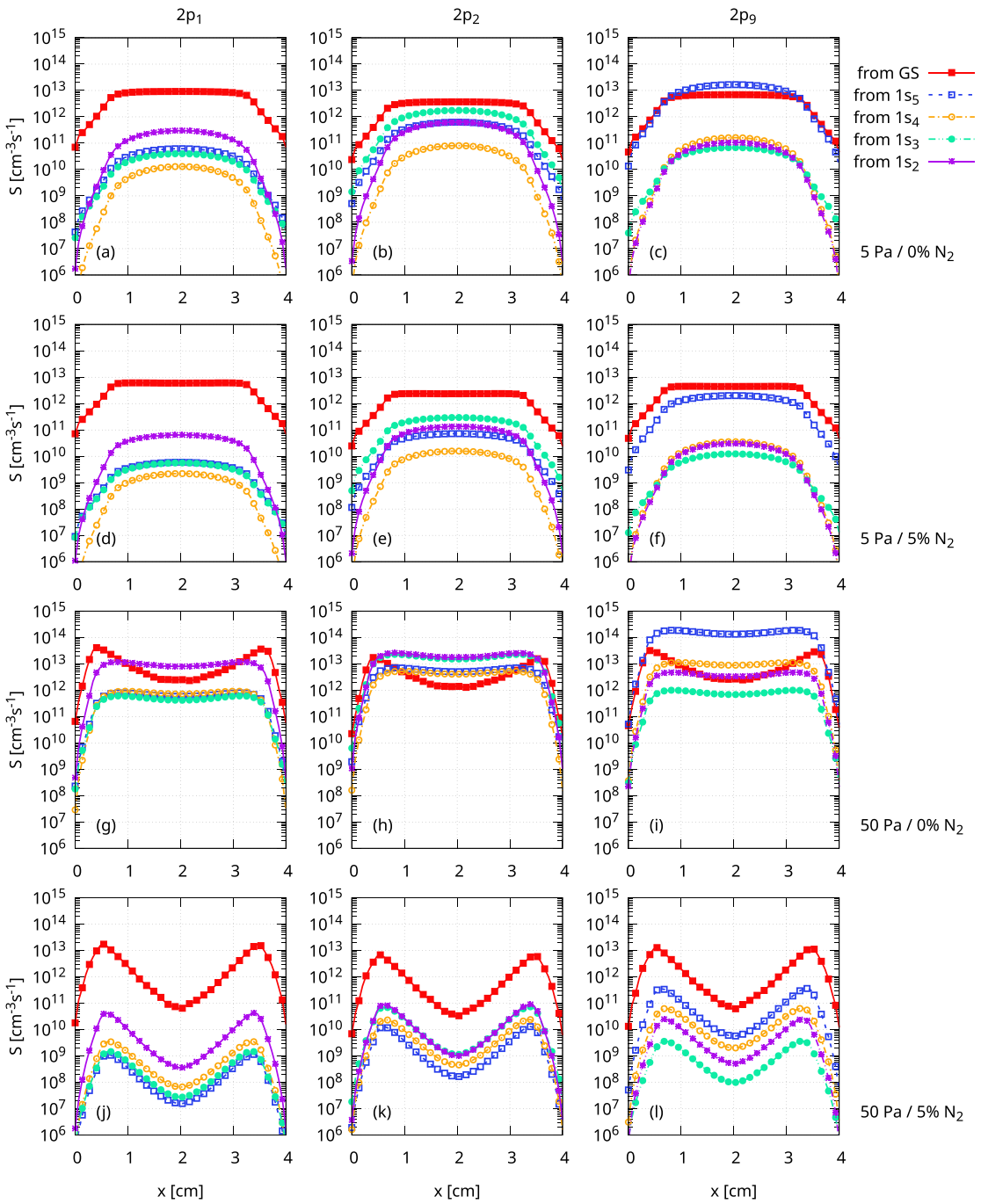


Figure 11. Excitation rates of selected 2p levels ($2p_1$: first column, $2p_2$: second column, and $2p_9$: third column) via direct (from ground state (GS)) and stepwise (from 1s levels) electron-impact excitation. Plots in the different rows correspond to specific combinations of the gas pressure (5 Pa and 50 Pa) and the N_2 content (0% and 5%). $V_{pp} = 300$ V. The powered electrode is situated at $x = 0$ cm, while the grounded electrode is at $x = 4$ cm.

from the $2p_1$ level). Note that the latter increase is only apparent, resulting by the relative decrease of many other lines that rely on step-wise excitation through the 1s levels. The 750.4 nm line itself, being predominantly determined by direct excitation from the ground state, is much less influenced by the N_2 content. This is a direct consequence of the different preferential populating mechanisms of the respective levels, as discussed above. The observed redistribution of the intensities of different lines, i.e. the changes in their ratios, means that in order to infer the plasma parameters from these lines, it is essential for CRMs to properly account for the quenching effect by the N_2 molecules. If the quenching is not included in the model, it will account only for the change in the EEPF (or effective electron temperature) and the electron density. As evidenced by the results in figure 12, this would result in vastly different line ratios entailing a significant misrepresentation of the underlying plasma parameters.

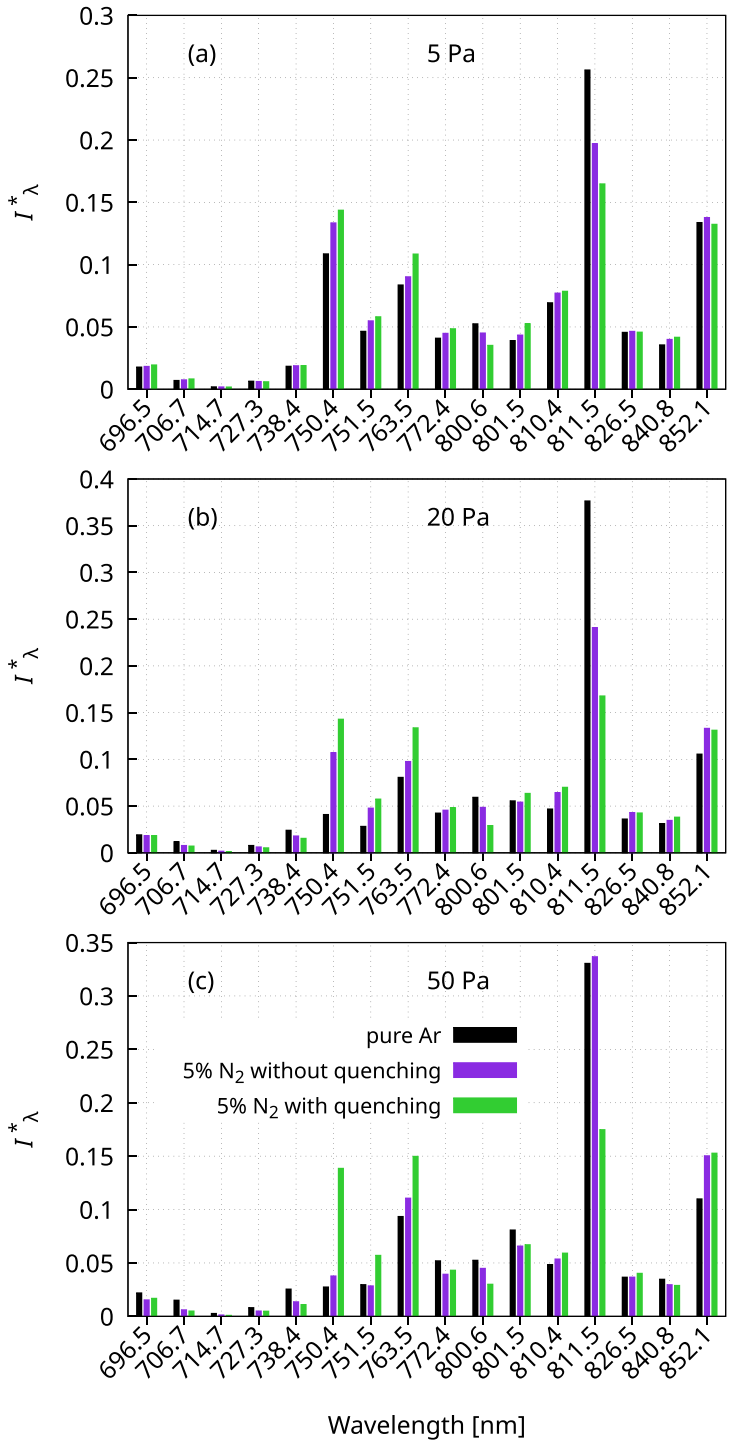


Figure 12. The effect of the changing EEPF and of the quenching process at 5% N_2 content, on the computed intensities of the Ar-I spectral lines at different values of the gas pressure, at the center of the discharge. The intensity values are normalized as $\sum I^*_\lambda = 1$. $V_{pp} = 300$ V.

The change of the EEPF is also most pronounced at the highest pressure, as figure 13 illustrates. At 50 Pa, the EEPF, even with an N_2 concentration as low as 1% takes the typical shape for nitrogen discharges [76], which shows a large electron population with energies below 2 eV, near the threshold energies of important vibrational excitation channels. The observed depletion of the energetic tail of the EEPF combined with the reduction in electron density as the N_2 content increases (figure 5) leads to a reduction of the excitation rate of the 1s levels. In a combination with increased losses via the quenching by N_2, this leads to the observed decrease of the densities of these levels (figure 9). The depletion of the EEPF of energetic electrons and the reduction in 1s level density ultimately explains the demonstrated behavior of the emission intensities.

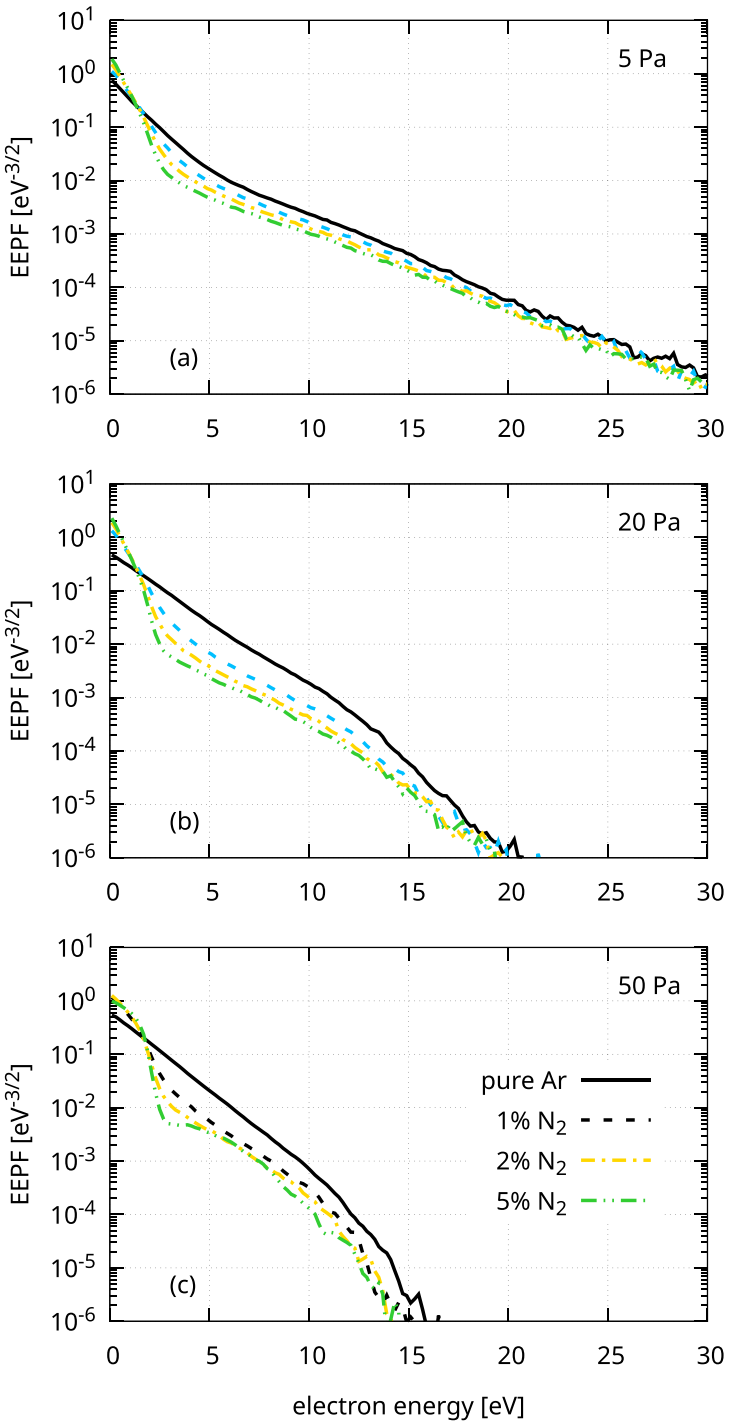


Figure 13. Effect of the N_2 content on the EEPF at the center of the discharge, at different values of the gas pressure. V_{pp} = 300 V.

5. Conclusions

A capacitively coupled radio-frequency discharge in Ar and Ar/N_2 mixtures was investigated both experimentally and computationally. The densities of Ar metastable species and the intensities of Ar-I 2p→1s spectral lines were compared, as a function of the N_2 admixture concentration. A fair agreement was found for both of these characteristics, within tolerances due to the simplification of the system geometry in the numerical framework. One also has to note that earlier works [77, 78] have pointed out possible accuracy issues in the cross section set used. Clarification of these issues remains for future work, as well as upgrading the treatment of radiation transport that was modeled here by an escape factor which is indeed a simplified way. An additional improvement could be the consideration of the excited level dynamics on N_2 molecules. Rotationally and vibrationally excited molecules may appear in considerable

amounts in the plasmas considered here and including them as targets of electron—N_2 collisions could make the modeling predictions more accurate.

Adding N_2 was found to lead to a decay of the densities of the metastable Ar species: at the lowest pressure of 2.5 Pa, the increase of N_2 concentration from 0% to 5% was found to result in a density drop of about a factor of two, for both the Ar $1s_5$ and $1s_3$ levels. At the highest pressure of 50 Pa, the same relative amount of nitrogen suppressed the metastable atom density by about two orders of magnitude. These changes, and similar variations of the densities of the Ar $1s_4$ and $1s_2$ (resonant) levels modify the excitation mechanism in a characteristic manner: while in the absence of N_2, the importance of the direct vs. stepwise electron-impact excitation varies for the specific 2p levels, via the depletion of the 1s levels, the presence of N_2 results in conditions where direct electron-impact excitation becomes dominant for all 2p levels. This change of dominant excitation mechanism results in marked alterations of the relative line intensities (I^*_λ), following a decrease in the electron density. At the same time, adding N_2 to the Ar gas results in a significant drop of all real line intensities (I_λ), due to increased electron 'cooling' in collisions with N_2. These trends were observed in both the experimental and computational data, in reasonably good agreement, considering again the uncertainties of the input data, the simplified geometry considered in the simulations and the approximate treatment of radiation transport.

Acknowledgments

This work was partially supported by Japan Science and Technology Agency (JST)'s 'Adopting Sustainable Partnerships for Innovative Research Ecosystem (ASPIRE)' Grant Number JPMJAP2321 and SICORP Grant Number JPMJSC2502. Ts. V. Ts. acknowledges the support by CNES Project R-S23/PF-0005-169-03 while carrying out this work within the joint laboratory COMHET, launched in 2023 by École Polytechnique, CNRS, Sorbonne Université, and Safran Electronics & Defense.

Data availability statement

The data that support the findings of this study are available upon reasonable request from the authors.

ORCID iDs

Zoltán Donkó 0000-0003-1369-6150
Simon Chouteau 0000-0001-8251-9735
Tsanko V Tsankov 0000-0002-7937-486X
Fatima Jenina Arellano 0000-0002-0543-6925
Satoshi Hamaguchi 0000-0001-6580-8797
Peter Hartmann 0000-0003-3572-1310

References

[1] Grigorian G, Dyatko N and Kochetov I 2018 *Plasma Phys. Rep.* **44** 1154–63
[2] Makabe T 2019 *J. Phys. D: Appl. Phys.* **52** 213002
[3] Hebner G A 1996 *J. Appl. Phys.* **80** 2624–36
[4] Yatom S, Chopra N, Kondeti S, Petrova T B, Raitses Y, Boris D R, Johnson M J and Walton S G 2023 *Plasma Sources Sci. Technol.* **32** 115005
[5] Tabassum N, Zafar A, Chan K, Chen T Y, Shannon S C and Bailliez L 2025 Role of nitrogen in modifying argon metastable dynamics in microwave-driven Ar-N_2 plasmas *78th Annual Gaseous Electronics Conf.*
[6] Zhu X M and Pu Y K 2010 *J. Phys. D: Appl. Phys.* **43** 403001
[7] Arellano F J, Kusaba M, Wu S, Yoshida R, Donkó Z, Hartmann P, Tsankov T V and Hamaguchi S 2024 *J. Vac. Sci. Technol. A* **42** 053001
[8] Dwivedi A and Hara K 2025 *J. Appl. Phys.* **58** 175203
[9] Donnelly V M 2004 *J. Phys. D: Appl. Phys.* **37** R217–36
[10] Akatsuka H 2009 *Phys. Plasmas* **16** 043502
[11] Iordanova S and Koleva I 2007 *Spectrochim. Acta B: At. Spectrosc.* **62** 344–56
[12] Bonaventura Z, Navrátil Z, Loffhagen D, Becker M M and Hoder T 2026 *Plasma Sources Sci. Technol.* **35** 025018
[13] Guerra V, Sá P and Loureiro J 2004 *Eur. Phys. J. Appl. Phys.* **28** 125–52
[14] Bibinov N, Kokh D, Kolokolov N, Kostenko V, Meyer D, Vinogradov I and Wiesemann K 1998 *Plasma Sources Sci. Technol.* **7** 298–309
[15] Kozlov K, Wagner H, Brandenburg R and Michel P 2001 *J. Phys. D: Appl. Phys.* **34** 3164–76
[16] Navrátil Z, Kusyn L, Prokop D and Hoder T 2025 *Plasma Sources Sci. Technol.* **34** 015013

[17] Bravo J, Rincón R, Muñoz J, Sánchez A and Calzada M 2015 *Plasma Chem. Plasma Process.* **35** 993–1014
[18] Lock E, Petrova T B, Petrov G, Boris D and Walton S 2016 *Phys. Plasmas* **23** 043518
[19] Vlcek J 1989 *J. Phys. D: Appl. Phys.* **22** 623–31
[20] Bogaerts A, Gijbels R and Vlcek J 1998 *J. Appl. Phys.* **84** 121–36
[21] Kano K, Suzuki M and Akatsuka H 2000 *Plasma Sources Sci. Technol.* **9** 314
[22] Schulze M, Yanguas-Gil A, Von Keudell A and Awakowicz P 2008 *J. Phys. D: Appl. Phys.* **41** 065206
[23] Akatsuka H 2019 *Adv. Phys. : X* **4** 1592707
[24] Chai K B and Kwon D H 2019 *J. Quant. Spectrosc. Radiat. Transfer* **227** 136–44
[25] Navrátil Z, Trunec D, Hrachová V and Kanka A 2007 *J. Phys. D: Appl. Phys.* **40** 1037–46
[26] Tsagkaridis M, Oliver T A, Fries D, O'Connor R, Barberena-Valencia J P, Raja L L, Varghese P L and Moser R D 2025 *Plasma Sources Sci. Technol.* **34** 105013
[27] Navrátil Z, Dvořák P, Brzobohaty O and Trunec D 2010 *J. Phys. D: Appl. Phys.* **43** 505203
[28] Toyoyoshi R, Sakamoto T, Matsuura H and Akatsuka H 2007 *Jpn. J. Appl. Phys.* **46** 3566
[29] Isola L M, López M, Cruceño J M and Gómez B 2014 *Plasma Sources Sci. Technol.* **23** 015014
[30] Foissac C, Krištof J, Annušová A, Veis P and Supiot P 2012 *Plasma Sources Sci. Technol.* **21** 055021
[31] Kang N, Gaboriau F, Oh S g and Ricard A 2011 *Plasma Sources Sci. Technol.* **20** 045015
[32] Gergs T, Mussenbrock T and Trieschmann J 2023 *J. Phys. D: Appl. Phys.* **56** 194001
[33] Duquenne C, Tessier P Y, Besland M P, Angleraud B, Jouan P Y, Aubry R, Delage S and Djouadi M 2008 *J. Appl. Phys.* **104** 063301
[34] Saikia P and Kakati B 2013 *J. Vac. Sci. Technol. A* **31** 061307
[35] Kovalsky S, Denisov V, Ostroverkhov E and Prokop'ev V 2023 *Russ. Phys. J.* **65** 1867–74
[36] Tu X, Chéron B, Yan J, Yu L and Cen K 2008 *Phys. Plasmas* **15** 053504
[37] Gaens W V, Iséni S, Schmidt-Bleker A, Weltmann K D, Reuter S and Bogaerts A 2015 *New J. Phys.* **17** 033003
[38] Deepak G D, Joshi N K, Prakash R and Pal U 2018 *Eur. Phys. J. Appl. Phys.* **83** 20801
[39] Šmíd P, Steers E B, Weiss Z and Vlček J 2003 *J. Anal. At. Spectrom.* **18** 549–56
[40] Šmíd P, Steers E, Weiss Z, Pickering J and Hoffmann V 2008 *J. Anal. At. Spectrom.* **23** 1223–33
[41] Simon P and Bogaerts A 2011 *J. Anal. At. Spectrom.* **26** 804–10
[42] Liang Y S, Xue C, Zhang Y R and Wang Y N 2021 *Phys. Plasmas* **28** 013510
[43] Huai Y, Li S Z, Li H, Wu K, Zhang J, Wang S and Wang Y X 2014 *IEEE Trans. Plasma Sci.* **42** 1648–53
[44] Yin G, Zhou Y and Yuan Q 2023 *Eur. Phys. J. Appl. Phys.* **98** 38
[45] Arellano F J, Gyulai M, Donkó Z, Hartmann P, Tsankov T V, Czarnetzki U and Hamaguchi S 2023 *Plasma Sources Sci. Technol.* **32** 125007
[46] Donkó Z, Hartmann P, Korolov I, Schulenberg D, Rohr S, Rauf S and Schulze J 2023 *Plasma Sources Sci. Technol.* **32** 065002
[47] Donkó Z, Tsankov T V, Hartmann P, Arellano F J, Czarnetzki U and Hamaguchi S 2024 *J. Appl. Phys.* **57** 375209
[48] Zatsarinny O, Wang Y and Bartschat K 2014 *Phys. Rev. A* **89** 022706
[49] Zatsarinny O 2006 *Comput. Phys. Commun.* **174** 273–356
[50] Zatsarinny O and Bartschat K 2013 *J. Phys. B: At. Mol. Opt. Phys.* **46** 112001
[51] BSR (www.lxcat.net/BSR)(Accessed 18 August 2022)
[52] Pitchford L C *et al* 2017 *Plasma Process. Polym.* **14** 1600098
[53] Carbone E, Graef W, Hagelaar G, Boer D, Hopkins M M, Stephens J C, Yee B T, Pancheshnyi S, van Dijk J and Pitchford L 2021 *Atoms* **9** 16
[54] Hyman H 1979 *Phys. Rev. A* **20** 855
[55] Lymberopoulos D P and Economou D J 1993 *J. Appl. Phys.* **73** 3668–79
[56] Phelps A V 1994 *J. Appl. Phys.* **76** 747–53
[57] Wen D Q, Krek J, Gudmundsson J T, Kawamura E, Lieberman M A and Verboncoeur J P 2021 *Plasma Sources Sci. Technol.* **30** 105009
[58] Press W, Flannery B, Teukolsky S, Vetterling W and Chipperfield J 1987 Numerical recipes: the art of scientific computing
[59] Siepa S L 2017 Global collisional-radiative model for optical emission spectroscopy of argon and argon-containing plasmas *Ph D Thesis Dissertation* Bochum, Ruhr-Universität Bochum
[60] Capriotti E R 1965 *Astrophys. J.* **142** 1101
[61] Bhatia A and Kastner S 2000 *J. Quant. Spectrosc. Radiat. Transfer* **67** 55–63
[62] Tachibana K 1986 *Phys. Rev. A* **34** 1007
[63] Sadeghi N, Setser D, Francis A, Czarnetzki U and Döbele H 2001 *J. Chem. Phys.* **115** 3144–54
[64] Chang R and Setser D 1978 *J. Chem. Phys.* **69** 3885–97
[65] Mewe R 1967 *Br. J. Appl. Phys.* **18** 107
[66] Biagi S F program, magboltz v. 8.97
[67] Biagi 8.97 database (available at: www.lxcat.net/Biagi) (Accessed 10 May 2024)
[68] Phelps A V 1991 *J. Phys. Chem. Ref. Data* **20** 557–73
[69] Olney T N, Cann N, Cooper G and Brion C 1997 *Chem. Phys.* **223** 59–98
[70] Amme R C and Hayden H C 1965 *J. Chem. Phys.* **42** 2011–5
[71] Spalburg M and Gislason E 1985 *Chem. Phys.* **94** 339–50
[72] Le Calve J, Gutcheck R and Dutuit O 1977 *Chem. Phys. Lett.* **47** 470–4
[73] Kim H, Iza F, Yang S, Radmilović-Radjenović M and Lee J 2005 *J. Phys. D: Appl. Phys.* **38** R283
[74] Lymberopoulos D P and Economou D J 1995 *J. Res. Natl Inst. Stand. Technol.* **100** 473
[75] Schulenberg D A, Korolov I, Donkó Z, Derzsi A and Schulze J 2021 *Plasma Sources Sci. Technol.* **30** 105003
[76] Pitchford L and Phelps A 1982 *Phys. Rev. A* **25** 540
[77] Carbone E, Hübner S, Van Der Mullen J, Kroesen G and Sadeghi N 2013 *J. Phys. D: Appl. Phys.* **46** 415202
[78] Carbone E, Van Veldhuizen E, Kroesen G and Sadeghi N 2015 *J. Phys. D: Appl. Phys.* **48** 425201